Article

Real-Time Monitoring of Strain Accumulation and Relief during Epitaxy of Ultrathin Co Ferrite Films with Varied Co Content

Jannis Thien [1], Jari Rodewald [1], Tobias Pohlmann [1,2], Kevin Ruwisch [1], Florian Bertram [2], Karsten Küpper [1] and Joachim Wollschläger [1,*]

[1] Department of Physics, Osnabrück University, 49076 Osnabrück, Germany; jthien@uos.de (J.T.); jari.rodewald@gmx.de (J.R.); pohlmann_t@t-online.de (T.P.); kruwisch@uos.de (K.R.); kkuepper@uos.de (K.K.)
[2] Deutsches Elektronen-Synchrotron (DESY), Photon Science, 22607 Hamburg, Germany; florian.bertram@desy.de
* Correspondence: jwollsch@uos.de; Tel.: +49-541-969-2651

Abstract: Ultrathin $Co_xFe_{3-x}O_4$ films of high structural quality and with different Co content (x = 0.6–1.2) were prepared by reactive molecular beam epitaxy on MgO(001) substrates. Epitaxy of these ferrite films is extensively monitored by means of time-resolved (operando) X-ray diffraction recorded in out-of-plane geometry to characterize the temporal evolution of the film structure. The Co ferrite films show high crystalline ordering and smooth film interfaces independent of their Co content. All $Co_xFe_{3-x}O_4$ films exhibit enhanced compressive out-of-plane strain during the early stages of growth, which partly releases with increasing film thickness. When the Co content of the ferrite films increases, the vertical-layer distances increase, accompanied by slightly increasing film roughnesses. The latter result is supported by surface-sensitive low-energy electron diffraction as well as X-ray reflectivity measurements on the final films. In contrast, the substrate–film interface roughness decreases with increasing Co content, which is confirmed with X-ray reflectivity measurements. In addition, the composition and electronic structure of the ferrite films is characterized by means of hard X-ray photoelectron spectroscopy performed after film growth. The experiments reveal the expected increasing Fe^{3+}/Fe^{2+} cation ratios for a higher Co content.

Keywords: cobalt ferrite; ultrathin films; strain; X-ray diffraction

1. Introduction

Among transition metal (TM) ferrites, the ferrimagnetic semiconductor $CoFe_2O_4$ (CFO) is a key material in the field of spintronics. For ultrathin epitaxial ferrite films, the strain induced by the lattice mismatch between the ferrite lattice and the substrate lattice is quite capable of leaving a great impact on several physical and chemical properties of ferrite films [1–5]. In particular, it has been reported that the strain in thinner ferrite films can modify the cationic distribution on different lattice sites [6], which in turn significantly affects, e.g., the electronic and magnetic properties of the ferrite films [1,7,8]. Therefore, substrate-induced strain can be specifically used for strain-engineering of ultrathin ferrite films to hugely improve the performance of ferrites for spintronic applications such as, e.g., spin-filters, where highly spin-polarized electrons are generated due to spin-dependent tunneling through ferrimagnetic barriers [9–12]. However, in order to tailor the properties of these ultrathin ferrite films using strain, it is important to know the details of strain accumulation, especially during the very early stages of growth, as well as strain relief during later growth stages [13]. Moreover, interfaces formed during the early stages of film growth are also crucial for the quality of devices based on, e.g., spin Hall magnetoresistance [14].

Hence, this work focuses on time-resolved (operando) X-ray diffraction (XRD) [13,15] to study the growth behavior and evolving strain of $Co_xFe_{3-x}O_4$ thin films with varying Co

content x = 0.6–1.2 up to a final film thickness of about 30 nm. The films are prepared using reactive molecular beam epitaxy (RMBE) with two individual sources for Fe and Co while deposition is performed in a diluted oxygen atmosphere to oxidize directly the deposited metals during deposition and to form Co ferrite films. The $Co_xFe_{3-x}O_4$ films were grown on MgO(001) substrates (lattice constant a_{MgO} = 421.2 pm) motivated by the small lattice mismatch of about -0.33% (comparing two unit cells of MgO with a single unit cell of CFO, lattice constant a_{CFO} = 839.2 pm). The latter agrees very well with the lattice constant $a_{Fe_3O_4}$ = 839.6 pm of magnetite (Fe_3O_4 being $Co_xFe_{3-x}O_4$ with $x = 0$), which has been studied here too for reasons of comparison. Thus, independent of the Co content of the Co ferrite films, almost-perfect growth conditions are guaranteed for $Co_xFe_{3-x}O_4$ thin films on MgO(001) due to the small lattice mismatch obtained for both Fe_3O_4 and $CoFe_2O_4$.

In addition to XRD, post-deposition structural characterization is performed by means of X-ray reflection (XRR) and low-energy electron diffraction (LEED) as well as electronic and magnetic characterization by means of hard X-ray photoelectron spectroscopy (HAXPES) to shed light on the surface and interface properties as well as on the electronic properties of the Co ferrite films and to obtain a more conclusive and comprehensive analysis.

2. Materials and Methods

Both the preparation and the in situ characterization of the $Co_xFe_{3-x}O_4$ films were carried out in an ultra-high-vacuum chamber with a base pressure of 1×10^{-10} mbar at beamline I07 [16] of the diamond light source (DLS). Prior to film deposition, the MgO(001) substrates were cleaned at a temperature of 400 °C in 5×10^{-5} mbar O_2 atmosphere to remove contaminating adsorbates (e.g., carbon) from the surfaces and to obtain well-defined surfaces [17]. The effectiveness of the cleaning process was examined with LEED.

$Co_xFe_{3-x}O_4$ films were grown by evaporating metals from pure Co and Fe rods in 5×10^{-6} mbar O_2 atmosphere, while keeping the substrates at a temperature of 250 °C. The metal rods (targets) were heated by exposing them directly to bombardment with electrons of high energy. It was demonstrated previously that ultrathin Fe_3O_4 films of high quality are formed on MgO(001) under these growth conditions [18]. In order to steer the stoichiometry of the resulting $Co_xFe_{3-x}O_4$ films, the Co flux was varied, whereas the Fe flux was kept constant. Additionally, one Fe_3O_4 film was grown under the same conditions for reasons of comparison.

During film growth, XRD measurements were continuously carried out in specular (θ–2θ) out-of-plane geometry close to the (002) and (004) Bragg conditions of MgO and $Co_xFe_{3-x}O_4$, respectively, to monitor the growth behavior of the ferrite films of different stoichiometry. Immediately after film deposition, LEED measurements and XRR measurements were performed at room temperature to examine the surface structure and crystallinity of the prepared $Co_xFe_{3-x}O_4$ film surfaces and to determine their final film thicknesses, respectively. Post-deposition XRD was also performed to examine a larger range of q-space in more detail not available in tr-XRD during deposition of the Co ferrite films. For the XRD and XRR measurements, a photon energy of 21 keV and a two-dimensional Pilatus 100K detector (Dectris AG, Baden, Switzerland) was used.

After film growth, HAXPES experiments were conducted at beamline P22 of PETRA III at Deutsches Elektronen-Synchrotron (DESY) (Hamburg, Germany) [19] and at 7-ID of the National Synchrotron Light Source II (NSLS-II) (Upton, NY, USA) [20] to examine the electronic structure and to determine the chemical composition of the $Co_xFe_{3-x}O_4$ films. Here, Co $2p$, Fe $2p$, and O $1s$ photoelectrons were excited by 6 keV photons in both studies.

The stoichiometry x of each film was determined by evaluating the relative intensity ratios of the Co $2p$ and Fe $2p$ spectra. The intensities were corrected by subtracting a Shirley background and normalized to the corresponding photoionization cross sections from Scofield [21] as well as to the corresponding inelastic mean free paths calculated by the Tanuma, Powell, and Penn formula (TPP-2M) [22]. In addition, the O content was obtained analogously by comparing the normalized intensities of O $1s$ photoelectrons with intensities obtained from Co and Fe cations. For all films, the obtained O stoichiometries

match with the expected O stoichiometry in $Co_xFe_{3-x}O_4$ (cation:anion = 4:3), indicating negligible anionic and/or cationic defects.

3. Results and Discussion

3.1. Operando tr-XRD during Film Growth

During deposition of the ferrite films, the XRD diffractograms were recorded in out-of-plane geometry to examine both the (002) Bragg reflection of the MgO substrate as well as the (004) Bragg peak of the evolving Co ferrite film. For operando XRD studies during growth of the Co ferrite films, Figure 1 exemplifies this experiment, showing XRD scans along the (00L) rods for different times during film growth of $Co_{0.9}Fe_{2.1}O_4$.
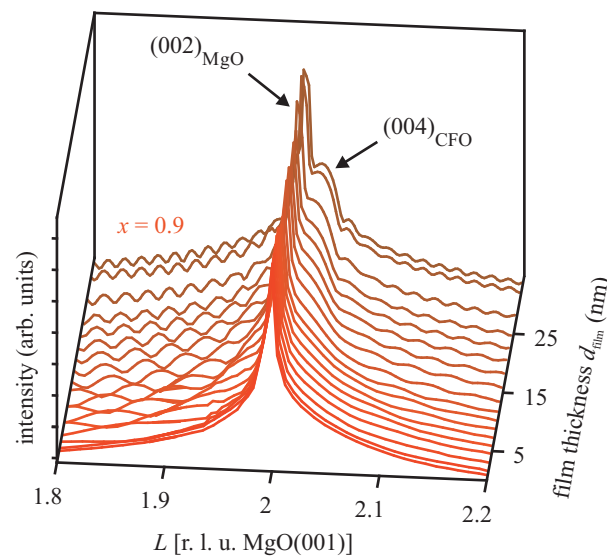

Figure 1. XRD scans in specular (θ–2θ) geometry close to the (002) Bragg peak of MgO. The (004) Bragg peak of the $Co_{0.9}Fe_{2.1}O_4$ film evolves during film deposition. Clear Laue oscillations are visible due to homogeneous film thickness and smooth interfaces.

Initially, the XRD scan of the pristine MgO(001) substrate shows exclusively a sharp and intense Bragg peak located at $L = 2$ corresponding to the (002) Bragg reflection of MgO with a rock-salt structure. Here L denotes the (vertical) scattering vector q scaled to the Bragg conditions of the MgO(001) substrate, namely, $L = qa_{MgO}/2\pi$. After the first few monolayers of $Co_{0.9}Fe_{2.1}O_4$ (~2 nm) are deposited on the MgO substrate, an initially very broad peak at slightly larger L values than the MgO(002) Bragg reflection becomes apparent as a shoulder. This can be ascribed to the evolving (004) Bragg reflection of $Co_{0.9}Fe_{2.1}O_4$ due to its (inverse) spinel structure and vertical-layer distance c_{vert} smaller than the MgO layer distance. With increasing coverage, the (004) Bragg reflection of $Co_{0.9}Fe_{2.1}O_4$ gains intensity and its FWHM decreases due to the growing thickness of the ferrite films. Moreover, Laue fringes emerge, pointing to the formation of high-quality ferrite films (homogeneous film thickness, high crystalline order).

Each XRD scan was analyzed in the framework of kinematical diffraction theory to determine the vertical-layer distance c_{vert}. The temporal evolution of the vertical-layer distance c_{vert} as obtained from this analysis is depicted in Figure 2 for $Co_xFe_{3-x}O_4$ films with varied Co content x.

The temporal evolution of the vertical-layer distances c_{vert} of the evolving film presented in Figure 2 shows that they are smaller than the layer distance $c_{CFO}^{250} = 210.3$ nm of bulk CFO at 250 °C for all $Co_xFe_{3-x}O_4$ films during the entire growth process. Here, thermal expansion of both the ferrite film and the MgO substrate has been considered to calculate the lattice constants at 250 °C from room temperature values [23]. Thus, the $Co_xFe_{3-x}O_4$ films are vertically compressively strained from the very first growth stages. Generally, this kind of compressive strain in the vertical direction is caused by

lateral tensile strain, which can be expected, e.g., considering lateral adaptation of the $Co_xFe_{3-x}O_4$ unit cell to the slightly larger unit cell of MgO(001) (pseudomorphic growth).
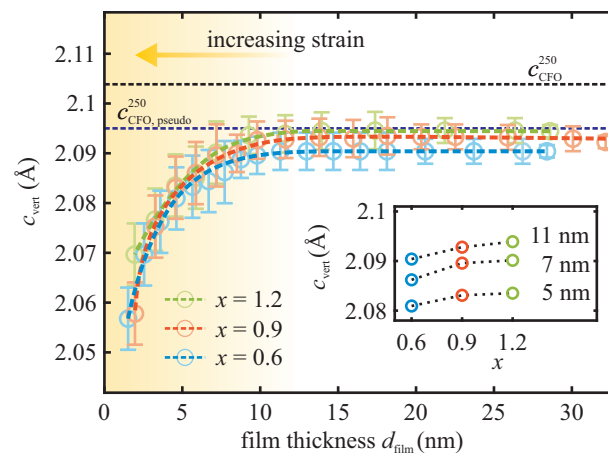

Figure 2. Temporal evolution of the vertical-layer distance c_{vert} during growth of $Co_xFe_{3-x}O_4$ films. The corresponding dashed lines serve as guides to the eye. The vertical-layer distance c_{CFO}^{250} of bulk CFO at 250 °C and the vertical-layer distance $c_{CFO, pseudo}^{250}$ of pseudomorphic CFO films grown at 250 °C are displayed for reference (dashed horizontal lines). Representative at three different $Co_xFe_{3-x}O_4$ film thicknesses, the inset shows the dependence of the evolving layer distances c_{vert} of the $Co_xFe_{3-x}O_4$ films on the Co content.

In general, the vertical induced strain $\Delta c_{vert}/c_{vert}$ caused by the lateral elastic distortion Δa_{lat} of the $Co_xFe_{3-x}O_4$ unit cells can be determined quantitatively according to Hashimoto et al. [24] via

$$\frac{\Delta c_{vert}}{c_{vert}} = \frac{2\nu}{\nu - 1}\frac{\Delta a_{lat}}{a_{lat}} \tag{1}$$

with the in-plane film lattice constant a_{lat} and $\nu = 0.367$ as the Poisson ration of CFO [25]. Assuming indeed a complete lateral adaptation of the $Co_xFe_{3-x}O_4$ lattice to the MgO(001) lattice and taking also into account the thermal expansion of both materials [23,26], a lateral strain of $\Delta a_{lat}/a_{CFO}^{250} = 0.35\%$ is expected, resulting in a vertical compressive strain of $\Delta c_{vert}/c_{CFO}^{250} = -0.41\%$ (cf. Figure 2).

The expected vertical compression of the films expected for pseudomorphic growth of CFO on MgO(001) is observed during the late stages of growth (film thickness $d_{film} > 12$ nm). For the early growth stages ($d_{film} < 12$ nm), however, the $Co_xFe_{3-x}O_4$ films show a significantly larger vertical compressive strain than expected and, thus, point to a large tensile lateral strain. Quite similar behavior has recently been observed in ultrathin $Ni_xFe_{3-x}O_4$ films ($0 \leq x \leq 1.5$) [13]. This effect has been attributed to the formation of antiphase boundaries (APBs) caused by the different crystal structure of the film (inverse spinel) and substrate (rock salt). It has been reported that the APBs significantly influence the strain properties of films [27,28]. APBs in the films lead to an increased lateral expansion and, consequently, to additional compressive vertical strain (cf. Equation (1)). With increasing film coverage, the compressive out-of-plane strain in each film diminishes constantly as the APB density decreases [29,30] until, finally, only a constant residual strain of $-0.5(\pm 0.1)\%$ remains at >12 nm film thickness. This residual strain is in accordance with the expected vertical strain of -0.41% assuming pseudomorphic growth (see above).

Due to the small lattice mismatch, the incorporation of strain-releasing misfit dislocations in the films would not be presumed to occur up to a critical film thickness. According to the model of Matthews and Blakeslee [31], the critical film thickness is ~87 nm for CFO films deposited on MgO(001). Thus, partial relaxation of the CFO films due to the injection of misfit dislocations is not expected here. Furthermore, we would like to point out that vertical compressive strain is decreasing with increasing Co content x in the $Co_xFe_{3-x}O_4$ films (cf. inset of Figure 2).

3.2. Post-Deposition Characterization

After film deposition, several experimental techniques were used to characterize the Co ferrite films in more detail. LEED, XRR and XRD experiments were performed in situ. Further HAXPES studies were carried out after the transfer of the samples through ambient conditions.

3.2.1. LEED

LEED images recorded at 150 eV electron energy directly after $Co_xFe_{3-x}O_4$ film growth are displayed in Figure 3. A typical LEED image of the pristine MgO(001) substrate after the cleaning procedure is displayed as well.
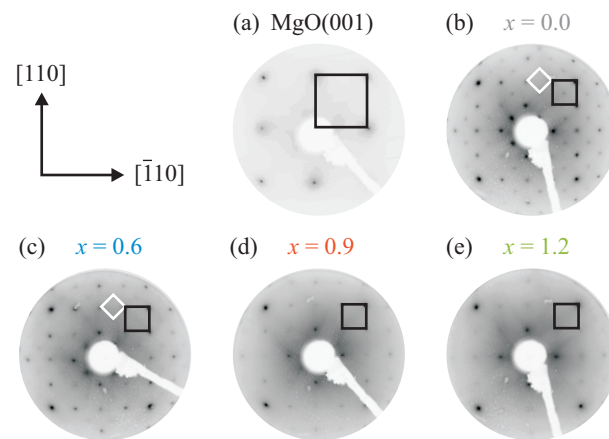

Figure 3. LEED pattern of the cleaned MgO(001) substrate and $Co_xFe_{3-x}O_4$ films recorded at an electron energy of 150 eV. The black squares indicate (1×1) surface unit cells of substrate and film. The white squares indicate the $(\sqrt{2} \times \sqrt{2})R45°$ superstructure unit cells.

The diffraction pattern of the cleaned MgO(001) substrate features a clear square (1×1) surface unit cell (reciprocal unit vectors point in the $[110]$ and $[\bar{1}10]$ directions) with sharp reflections and a low background intensity, indicating a well-ordered and crystalline MgO(001) surface with a low defect density.

For the $Co_xFe_{3-x}O_4$ film with $x = 0$ (magnetite, Fe_3O_4), the LEED pattern also shows a clear square fundamental (1×1) surface unit cell with $Fe_3O_4 \langle 110 \rangle \| MgO \langle 110 \rangle$. The reciprocal surface unit cell of Fe_3O_4 is approximately two times smaller than the surface unit cell of MgO(001) in both crystallographic directions due to the almost doubled size of the surface unit cell of Fe_3O_4(001) compared to the unit cell of MgO(001). Additionally, a $(\sqrt{2} \times \sqrt{2})R45°$ superstructure is visible, which is typical for well-ordered Fe_3O_4 surfaces [32–34].

As the Co content x in the $Co_xFe_{3-x}O_4$ films increases, the intensity of the $(\sqrt{2} \times \sqrt{2})R45°$ superstructure diffraction pattern decreases until it vanishes completely for $x > 0.6$. The diffraction pattern of the fundamental (1×1) structure, however, shows intense and sharp diffraction peaks. This result is in excellent agreement with earlier studies demonstrating that the surface of $CoFe_2O_4$(001) films is not reconstructed [35]. Furthermore, a marginal increase in the background intensity with increasing Co content is observable, pointing to a slightly increasing density of surface defects for the $Co_xFe_{3-x}O_4$ films with a higher Co content.

3.2.2. XRR

The X-ray reflectivity scans of all $Co_xFe_{3-x}O_4$ films recorded directly after film deposition are depicted in Figure 4. All reflectivity curves exhibit clear intensity oscillations (Kiessig fringes) due to interference of the beams reflected from the smooth film surface and substrate–film interfaces pointing to sharp interfaces. In each reflectivity curve, the intensity oscillations show only one periodicity, indicating the formation of single $Co_xFe_{3-x}O_4$ films of 30($\pm$2) nm thickness (cf. Table 1 for more details). The oscillations are most strongly

attenuated for the $Co_xFe_{3-x}O_4$ film with the lowest Co content of $x = 0.6$. The Kiessig fringes are more prominent for the pure magnetite film and for Co ferrite films with a higher Co content. Thus, it can be concluded that the interface roughness decreases with increasing Co content.
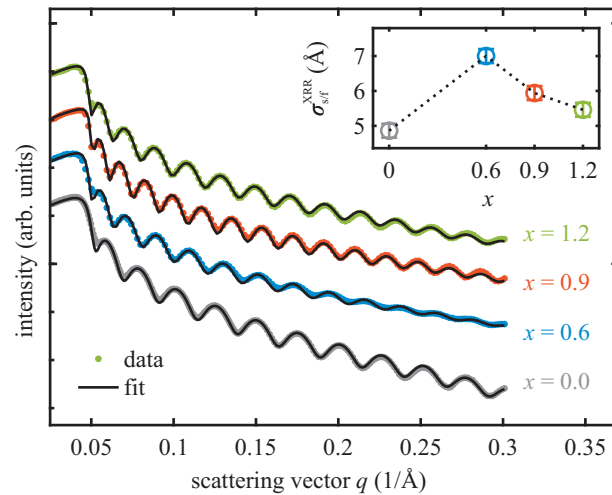

Figure 4. Reflectivity curves and respective fits (black solid lines) for varied $Co_xFe_{3-x}O_4$ films with different Co content ($0 \leq x \leq 1.2$). The inset shows the interface roughness $\sigma_{s/f}^{XRR}$ between MgO substrate and each $Co_xFe_{3-x}O_4$ film extracted from the respective fits.

The reflectivity curves were analyzed according to the Parratt algorithm [36] and the Névot–Croce roughness model [37]. For comparison, the corresponding calculated reflectivity curves (black lines) are shown in Figure 4 as well. The fits are based on a single-film-plus-substrate model, in which the film thickness, interface roughness and refractive indices are fitting parameters. For the refractive index of the MgO substrate, literature values [38] were used, whereas for the refractive indices of the $Co_xFe_{3-x}O_4$ films a deviation of $\pm 5\%$ from the reported value for bulk CFO [38] was allowed. The calculated reflectivity curves agree well with the experimental data for all samples. This confirms the applied model and the formation of single $Co_xFe_{3-x}O_4$ films. The dependence of the interface roughness $\sigma_{s/f}^{XRR}$ on different Co content is presented in Figure 4. It has its maximum for $x = 0.6$, while it decreases with increasing Co content as already discussed qualitatively before considering the attenuation of the Kiessig fringes.

3.2.3. Post-Deposition XRD

Figure 5 presents the experimental XRD data of different $Co_xFe_{3-x}O_4$ films recorded directly after film growth. The (004) Bragg reflections of the $Co_xFe_{3-x}O_4$ films shift closer to the (002) Bragg reflection of MgO as the Co content increases, indicating a continuously increasing vertical-layer distance with increasing Co content (cf. inset of Figure 5). All films are nearly atomically flat, as demonstrated by the well-developed Laue fringes.

For quantitative analysis, XRD diffractograms were additionally calculated via kinematic diffraction theory, also shown as black lines in Figure 5. They were optimized while varying the structural parameters such as, e.g., the vertical-layer distance c_{vert} as well as the roughness σ_f^{XRD} and $\sigma_{s/f}^{XRD}$ of the film surface and substrate–film interface, respectively. The calculated diffractograms agree well with the experimental data. The respective structural parameters are presented in Table 1. In accordance with the LEED analysis, the surface roughness σ_f^{XRD} is very small and the interface roughness $\sigma_{s/f}^{XRD}$ obtained using XRD is in excellent agreement with those concluded from XRR (cf. Figure 4).
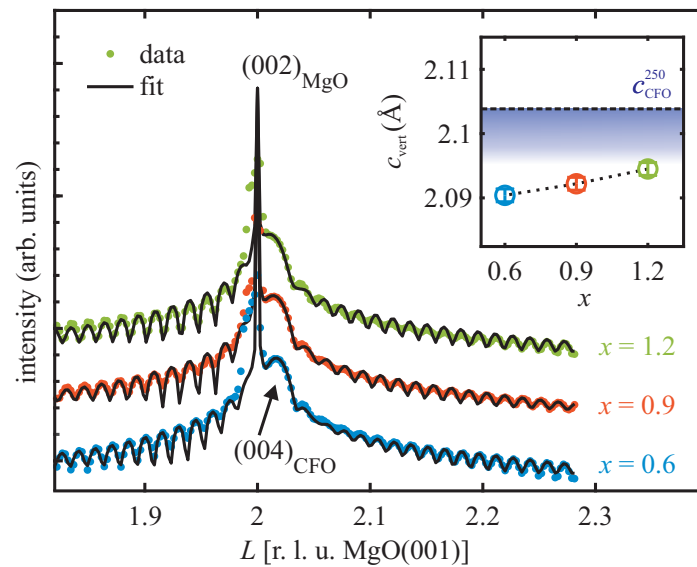
Figure 5. XRD scans (dots) of $Co_xFe_{3-x}O_4$ film ($x \geq 0.6$) recorded after deposition at 250 °C. Corresponding diffractograms calculated using kinematic diffraction theory (black solid lines) are also shown. The obtained vertical-layer distances c_{vert} are presented in the inset. The horizontal dashed line in the inset marks the vertical-layer distance c_{CFO}^{250} of bulk CFO at 250 °C considering thermal expansion. All films are vertically compressed with decreasing compression for increasing Co content.

Table 1. Structural parameters of the prepared $Co_xFe_{3-x}O_4$ films. The final $Co_xFe_{3-x}O_4$ film thickness d_{film}^{XRR} was determined with XRR, while the vertical-layer distance c_{vert}, the film surface roughness σ_f^{XRD} and the substrate–film interface roughness $\sigma_{s/f}^{XRD}$ were determined from the XRD analysis based on kinematic diffraction theory.

Co Content x	d_{film}^{XRR} (nm)	c_{vert} (pm)	σ_f^{XRD} (pm)	$\sigma_{s/f}^{XRD}$ (pm)
0.6	28.2 ± 0.2	209.0 ± 0.1	60 ± 20	710 ± 30
0.9	32.1 ± 0.2	209.2 ± 0.1	70 ± 20	670 ± 30
1.2	28.6 ± 0.2	209.5 ± 0.1	70 ± 20	630 ± 30

3.3. HAXPES

The Co $2p$ and Fe $2p$ core-level spectra of the HAXPES measurements of previously prepared $Co_xFe_{3-x}O_4$ films recorded after deposition and sample transfer under ambient conditions are shown in Figure 6. The spectra were calibrated according to the O $1s$ core-level at 530 eV [39,40]. All spectra show $2p_{1/2}$ and $2p_{3/2}$ photoelectron peaks as a result of spin-orbit coupling.

All Co $2p$ core-level spectra of the $Co_xFe_{3-x}O_4$ films with $x \geq 0.6$ show two main peaks (Co $2p_{1/2}$ and Co $2p_{3/2}$), which are located at binding energies of about 795.8 eV and 780.0 eV, respectively. As expected, there is no Co $2p$ signal for the Fe_3O_4 film ($x = 0$, cf. gray line in Figure 6a). Each main peak is accompanied by one (shake-up) satellite peak at $\sim$6 eV higher binding energies characteristic for divalent Co cations [35,41,42]. The shape of the presented Co $2p$ spectra is therefore consistent with Co^{2+} incorporated in ferrite films [35].

The Fe $2p$ core-level spectrum of the magnetite film ($x = 0$) reveals two main peaks of Fe $2p_{1/2}$ and Fe $2p_{3/2}$ at binding energies of about 723.8 eV and 710.3 eV, respectively. The Fe $2p_{3/2}$ peak also shows a shoulder at its lower-binding-energy side due to the presence of Fe^{2+} cations [43]. Furthermore, no *apparent* (charge-transfer) satellite can be observed between the Fe $2p_{1/2}$ and Fe $2p_{3/2}$ peaks. This effect is attributed to mixed Fe^{3+} and Fe^{2+} valence states, known well from magnetite [39].

As the Co content in the $Co_xFe_{3-x}O_4$ films increases ($x > 0$), both the Fe $2p_{1/2}$ peak and Fe $2p_{3/2}$ peak shift to higher binding energies. In addition, the Fe^{2+}-related shoulder vanishes for higher Co content while Fe^{3+} charge-transfer satellites at ~719.0 eV and ~733.0 eV become visible. All three observations point to increasing Fe^{3+}/Fe^{2+} ratios and are expected for cobalt ferrite films with increasing Co content due to the substitution of Fe^{2+} by Co^{2+} [44].
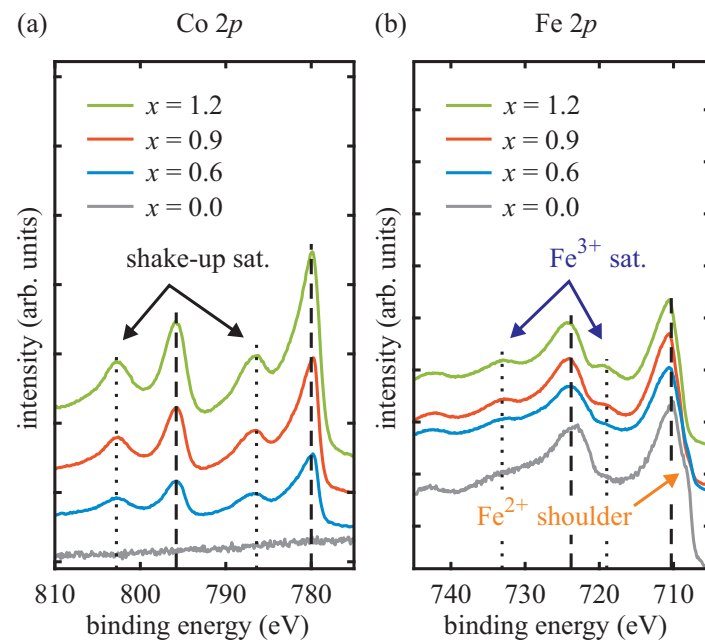

Figure 6. (**a**) Co $2p$ and (**b**) Fe $2p$ core-level spectra of $Co_xFe_{3-x}O_4$ films with different Co content. Dotted black lines indicate the positions of Co^{2+} shake-up satellites in (**a**) and the positions of the Fe^{3+} charge-transfer satellite peaks in (**b**). Dashed black lines indicate the positions of the respective main peaks for CFO ($x = 1$) in (**a**) and for magnetite ($x = 0$) in (**b**).

4. Conclusions

In summary, the growth behavior and evolving strain of $Co_xFe_{3-x}O_4$ single thin films with stoichiometries $x = 0.6$–1.2 grown on MgO(001) were monitored with operando time-resolved specular XRD measurements, which were analyzed using full kinematic diffraction theory. For each film, highly crystalline ordering is observed throughout the entire film growth. However, up to a film thickness of $d_{film} \sim 12$ nm, all $Co_xFe_{3-x}O_4$ films exhibited enhanced vertical compressive strain attributed to the formation of APBs during the growth of the Co ferrite films on MgO(001). The strain, however, partly releases with increasing film thickness. The residual constant vertical strain for film thicknesses above 12 nm is reconcilable with the model of pseudomorphic growth on MgO substrates. Furthermore, the vertical-layer distance of the $Co_xFe_{3-x}O_4$ films increases with increasing Co content, while all films exhibit overall very small surface roughnesses. Nevertheless, LEED measurements point to a slight increase in the surface defect density with increasing Co content. In contrast to this, the roughness of the substrate–film interface decreases for increasing Co content, as indicated in both the XRR and XRD analyses. HAXPES experiments confirm the underlying stoichiometry of the $Co_xFe_{3-x}O_4$ films and reveal a reduced amount of Fe^{2+} cations for higher x due to the expected gradual substitution of Fe^{2+} by Co^{2+}.

Finally, considering the evolving strain of the different $Co_xFe_{3-x}O_4$ films produced, our results may open up new perspectives for strain engineering physical properties of ultrathin $Co_xFe_{3-x}O_4$ films depending on the amounts of Co. Accurate knowledge of the strain accumulation in the films as provided here allows specific physical (magnetic or electronic) properties to be targeted to meet or even surpass the criteria required for the

films to be used in spintronics. For instance, it has to be explored how the APB-related strain influences the electronic structure, e.g., the spin-dependent band gap and, thus, the use of ultrathin Co ferrite films as spin-filters.

Conflicts of Interest: The authors declare no conflict of interest. The funders had no role in the design of the study; in the collection, analyses, or interpretation of data; in the writing of the manuscript; or in the decision to publish the results.

References

1. Moyer, J.A.; Kumah, D.P.; Vaz, C.A.F.; Arena, D.A.; Henrich, V.E. Epitaxial strain-induced changes in the cation distribution and resistivity of Fe-doped $CoFe_2O_4$. *Appl. Phys. Lett.* **2012**, *101*, 021907. [CrossRef]
2. Tainosho, T.; Inoue, J.-I.; Sharmin, S.; Takeguchi, M.; Kita, E.; Yanagihara, H. Large negative uniaxial magnetic anisotropy in highly distorted Co-ferrite thin films. *Appl. Phys. Lett.* **2019**, *114*, 092408. [CrossRef]
3. Wisser, J.J.; Riddiford, L.J.; Altman, A.; Li, P.; Emori, S.; Shafer, P.; Klewe, C.; N'Diaye, A.T.; Arenholz, E.; Suzuki, Y. The role of iron in magnetic damping of $Mg(Al,Fe)_2O_4$ spinel ferrite thin films. *Appl. Phys. Lett.* **2020**, *116*, 142406. [CrossRef]
4. Regmi, S.; Li, Z.; Srivastava, A.; Mahat, R.; KC, S.; Rastogi, A.; Galazka, Z.; Datta, R.; Mewes, T.; Gupta, A. Structural and magnetic properties of $NiFe_2O_4$ thin films grown on isostructural lattice-matched substrates. *Appl. Phys. Lett.* **2021**, *118*, 152402. [CrossRef]
5. Rigato, F.; Geshev, J.; Skumryev, V.; Fontcuberta, J. The magnetization of epitaxial nanometric $CoFe_2O_4$ (001) layers. *J. Appl. Phys.* **2009**, *106*, 113924. [CrossRef]
6. Rodewald, J.; Thien, J.; Ruwisch, K.; Bertram, F.; Kuepper, K.; Wollschläger, J. Enhanced magnetization of ultrathin $NiFe_2O_4$ films on $SrTiO_3$(001) related to cation disorder and anomalous strain. *Phys. Rev. Mater.* **2020**, *4*, 064404. [CrossRef]
7. Zviagin, V.; Kumar, Y.; Lorite, I.; Esquinazi, P.; Grundmann, M.; Schmidt-Grund, R. Ellipsometric investigation of $ZnFe_2O_4$ thin films in relation to magnetic properties. *Appl. Phys. Lett.* **2016**, *108*, 131901. [CrossRef]
8. Lüders, U.; Bibes, M.; Bobo, J.F.; Cantoni, M.; Bertacco, R.; Fontcuberta, J. Enhanced magnetic moment and conductive behavior in $NiFe_2O_4$ spinel ultrathin films. *Phys. Rev. B* **2005**, *71*, 134419. [CrossRef]
9. Moussy, J.B. From epitaxial growth of ferrite thin films to spin-polarized tunnelling. *J. Phys. D Appl. Phys.* **2013**, *46*, 143001. [CrossRef]
10. Takahashi, Y.K.; Kasai, S.; Furubayashi, T.; Mitani, S.; Inomata, K.; Hono, K. High spin-filter efficiency in a Co ferrite fabricated by a thermal oxidation. *Appl. Phys. Lett.* **2010**, *96*, 072512. [CrossRef]
11. Lukashev, P.V.; Burton, J.D.; Smogunov, A.; Velev, J.P.; Tsymbal, E.Y. Interface states in $CoFe_2O_4$ spin-filter tunnel junctions. *Phys. Rev. B* **2013**, *88*, 134430. [CrossRef]
12. Tezuka, N. New materials research for high spin polarized current. *J. Magn. Magn. Mater.* **2012**, *324*, 3588–3592. [CrossRef]

13. Rodewald, J.; Thien, J.; Pohlmann, T.; Hoppe, M.; Bertram, F.; Kuepper, K.; Wollschläger, J. Real-time monitoring the growth of strained off-stoichiometric $Ni_xFe_{3-x}O_4$ ultrathin films on MgO(001). *Appl. Phys. Lett.* **2020**, *117*, 011601. [CrossRef]

14. Althammer, M.; Singh, A.V.; Wimmer, T.; Galazka, Z.; Huebl, H.; Opel, M.; Gross, R.; Gupta, A. Role of interface quality for the spin Hall magnetoresistance in nickel ferrite thin films with bulk-like magnetic properties. *Appl. Phys. Lett.* **2019**, *115*, 092403. [CrossRef]

15. Kuschel, O.; Spiess, W.; Schemme, T.; Rubio-Zuazo, J.; Kuepper, K.; Wollschläger, J. Real-time monitoring of the structure of ultrathin Fe_3O_4 films during growth on Nb-doped $SrTiO_3$(001). *Appl. Phys. Lett.* **2017**, *111*, 041902. [CrossRef]

16. Nicklin, C.; Arnold, T.; Rawle, J.; Warne, A. Diamond beamline I07: A beamline for surface and interface diffraction. *J. Synchrotron Rad.* **2016**, *23*, 1245–1253. [CrossRef]

17. Schemme, T.; Krampf, A.; Bertram, F.; Kuschel, T.; Kuepper, K.; Wollschläger, J. Modifying magnetic properties of ultra-thin magnetite films by growth on Fe pre-covered MgO(001). *J. Appl. Phys.* **2015**, *118*, 113904. [CrossRef]

18. Bertram, F.; Deiter, C.; Schemme, T.; Jentsch, S.; Wollschläger, J. Reordering between tetrahedral and octahedral sites in ultrathin magnetite films grown on MgO(001). *J. Appl. Phys.* **2013**, *113*, 184103. [CrossRef]

19. Schlueter, C.; Gloskovskii, A.; Ederer, K.; Schostak, I.; Piec, S.; Sarkar, I.; Matveyev, Y.; Lömker, P.; Sing, M.; Claessen, R.; et al. The new dedicated HAXPES beamline P22 at PETRAIII. *AIP Conf. Proc.* **2019**, *2054*, 040010. [CrossRef]

20. Weiland, C.; Jaye, C.; Quackenbush, N.F.; Gann, E.; Fu, Z.; Kirkland, J.P.; Karlin, B.A.; Ravel, B.; Woicik, J.C.; Fischer, D.A. NIST HAXPES at NSLS and NSLS-II. *Synchrotron Rad. News* **2018**, *31*, 23–28. [CrossRef]

21. Scofield, J.H. *Theoretical Photoionization Cross Sections from 1 to 1500 keV*; Technical Report, UCRL-51326; California University: Los Angeles, CA, USA; Lawrence Livermore Laboratory: Livermore, CA, USA, 1973. [CrossRef]

22. Tanuma, S.; Powell, C.J.; Penn, D.R. Calculation of electron inelastic mean free paths (IMFPs) VII. Reliability of the TPP2M IMFP predictive equation. *Surf. Interface Anal.* **2003**, *35*, 268–275. [CrossRef]

23. Iyengar, L.; Prasad, B.R.; Qadri, B. Thermal Expansion of Cobalt Ferrite and Cobalt-Zinc Ferrite. *Curr. Sci.* **1973**, *42*, 534–535.

24. Hashimoto, S.; Peng, J.L.; Gibson, W.M. Strain measurement of epitaxial CaF_2 on Si(111) by MeV ion channeling. *Appl. Phys. Lett.* **1985**, *47*, 1071–1073. [CrossRef]

25. Foerster, M.; Iliev, M.; Dix, N.; Martí, X.; Barchuk, M.; Sánchez, F.; Fontcuberta, J. The Poisson Ratio in $CoFe_2O_4$ Spinel Thin Films. *Adv. Funct. Mater.* **2012**, *22*, 4344–4351. [CrossRef]

26. Durand, M.A. The Coefficient of Thermal Expansion of Magnesium Oxide. *Physics* **1936**, *7*, 297–298. [CrossRef]

27. Arora, S.K.; Sofin, R.G.S.; Shvets, I.V.; Luysberg, M. Anomalous strain relaxation behavior of Fe_3O_4/MgO(100) heteroepitaxial system grown using molecular beam epitaxy. *J. Appl. Phys.* **2006**, *100*, 073908. [CrossRef]

28. Balakrishnan, K.; Arora, S.K.; Shvets, I.V. Strain relaxation studies of the Fe_3O_4/MgO(100) heteroepitaxial system grown by magnetron sputtering. *J. Phys. Condens. Matter* **2004**, *16*, 5387–5393. [CrossRef]

29. Eerenstein, W.; Palstra, T.T.M.; Hibma, T.; Celotto, S. Diffusive motion of antiphase domain boundaries in Fe_3O_4 films. *Phys. Rev. B* **2003**, *68*, 014428. [CrossRef]

30. Ramos, A.V.; Moussy, J.B.; Guittet, M.J.; Bataille, A.M.; Gautier-Soyer, M.; Viret, M.; Gatel, C.; Bayle-Guillemaud, P.; Snoeck, E. Magnetotransport properties of Fe_3O_4 epitaxial thin films: Thickness effects driven by antiphase boundaries. *J. Appl. Phys.* **2006**, *100*, 103902. [CrossRef]

31. Matthews, J.W.; Blakeslee, A.E. Defects in epitaxial multilayers: I. Misfit dislocations. *J. Cryst. Growth* **1974**, *27*, 118. [CrossRef].

32. Bliem, R.; McDermott, E.; Ferstl, P.; Setvin, M.; Gamba, O.; Pavelec, J.; Schneider, M.A.; Schmid, M.; Diebold, U.; Blaha, P.; et al. Subsurface cation vacancy stabilization of the magnetite (001) surface. *Science* **2014**, *346*, 1215–1218. [CrossRef]

33. Korecki, J.; Handke, B.; Spiridis, N.; Ślęzak, T.; Flis-Kabulska, I.; Haber, J. Size effects in epitaxial films of magnetite. *Thin Solid Films* **2002**, *412*, 14–23. [CrossRef]

34. Pentcheva, R.; Moritz, W.; Rundgren, J.; Frank, S.; Schrupp, D.; Scheffler, M. A combined DFT/LEED-approach for complex oxide surface structure determination: Fe_3O_4(001). *Surf. Sci.* **2008**, *602*, 1299–1305. [CrossRef]

35. Chambers, S.; Farrow, R.; Maat, S.; Toney, M.; Folks, L.; Catalano, J.; Trainor, T.; Brown, G.E., Jr. Molecular beam epitaxial growth and properties of $CoFe_2O_4$ on MgO(001). *J. Magn. Magn. Mater.* **2002**, *246*, 124–139. [CrossRef]

36. Parratt, L.G. Surface Studies of Solids by Total Reflection of X-rays. *Phys. Rev.* **1954**, *95*, 359–369. [CrossRef]

37. Névot, L.; Croce, P. Caractérisation des surfaces par réflexion rasante de rayons X. Application à l'étude du polissage de quelques verres silicates. *Róev. Phys. Appl.* **1980**, *15*, 761–779. [CrossRef]

38. Henke, B.L.; Gullikson, E.M.; Davis, J.C. X-ray Interactions: Photoabsorption, Scattering, Transmission, and Reflection at E = 50–30,000 eV, Z = 1–92. *At. Data Nucl. Data Tables* **1993**, *54*, 181–342. [CrossRef]

39. Yamashita, T.; Hayes, P. Analysis of XPS spectra of Fe^{2+} and Fe^{2+} ions in oxide materials. *Appl. Surf. Sci.* **2008**, *254*, 2441–2449. [CrossRef]

40. Allen, G.C.; Curtis, M.T.; Hooper, A.J.; Tucker, P.M. X-ray photoelectron spectroscopy of iron-oxygen systems. *J. Chem. Soc. Dalton Trans.* **1974**, *14*, 1525–1530. [CrossRef]

41. Shen, Z.X.; Allen, J.W.; Lindberg, P.A.P.; Dessau, D.S.; Wells, B.O.; Borg, A.; Ellis, W.; Kang, J.S.; Oh, S.J.; Lindau, I.; et al. Photoemission study of CoO. *Phys. Rev. B* **1990**, *42*, 1817–1828. [CrossRef]

42. McIntyre, N.S.; Cook, M.G. X-ray photoelectron studies on some oxides and hydroxides of cobalt, nickel, and copper. *Anal. Chem.* **1975**, *47*, 2208–2213. [CrossRef]

43. Biesinger, M.C.; Payne, B.P.; Grosvenor, A.P.; Lau, L.W.M.; Gerson, A.R.; Smart, R.S.C. Resolving surface chemical states in XPS analysis of first row transition metals, oxides and hydroxides: Cr, Mn, Fe, Co and Ni. *Appl. Surf. Sci.* **2011**, *257*, 2717–2730. [CrossRef]

44. Moyer, J.A.; Vaz, C.A.F.; Negusse, E.; Arena, D.A.; Henrich, V.E. Controlling the electronic structure of $Co_{1-x}Fe_{2+x}O_4$ thin films through iron doping. *Phys. Rev. B* **2011**, *83*, 035121. [CrossRef]